A 'Violin-Mode' shadow sensor for interferometric gravitational wave detectors

N.A. Lockerbie and K.V. Tokmakov

SUPA (Scottish Universities Physics Department) Department of Physics, University of Strathclyde, 107 Rottenrow, Glasgow G4 0NG, UK

Abstract. This paper describes a system of four novel shadow detectors having, collectively, a displacement sensitivity of (69 ± 13) pm_{rms} / √Hz, at 500 Hz, over a measuring span of ±0.1 mm. The detectors were designed to monitor so-called 'Violin-Mode' (*VM*) Eigenmode resonances in the 600 mm long by 400 μm diameter silica suspension fibres of the test-masses/mirrors for the advanced LIGO (Laser Interferometer Gravitational wave Observatory) gravitational wave detectors. These modes may be excited by earthquake or mechanical relaxation events, and the fibres then can transfer vibrational energy to the suspended test masses within the gravitational wave detection bandwidth. The fibres' ring-down time under vacuum, i.e., the consequential interferometer dead-time, is measured in days, as the *VM* resonances slowly decay away, and consequently these modes must be detected and then (cold-) damped. The *VM* detection system described here had a target sensitivity of 10^{-10} m (rms)/√Hz at 500 Hz, together with, ultimately, a required detection span of ±0.1 mm about the mean position of each fibre—in order to compensate for potential slow drift over time of fibre position, due to mechanical relaxation. The full sensor system, comprising emitters (sources of illumination) and shadow detectors, therefore met these specifications, and, using these sensors, *VM* resonances having amplitudes of 1.2 nm, rms, were detected in the suspension fibres of an advanced LIGO dummy test-mass. This paper focuses mainly on the detector side of the shadow-sensors. The emitters are described in an accompanying paper.

PACS number: 0480

1. Introduction

In the advanced LIGO 'aLIGO' ground-based interferometric gravitational wave detectors, each essentially cylindrical 40 kg test-mass/mirror is to be suspended in vacuum from a multi-stage pendulum seismic isolation system [1–3]. The suspended mirrors' cylindrical axes are to be orientated horizontally, and the final (lowest) stage of each such suspension will comprise four fused-silica suspension fibres of circular cross-section attached to the test-mass/mirror itself, each fibre measuring approximately 600 mm long by 400 μm in diameter [4, 5]. Stability of the interferometers' 4 km arms (formed by pairs of such suspended mirrors) is to be provided by a system of sensors and actuators, intended to compensate for drifts in, and excitations of, the suspension [6].

The lateral Eigenmodes, or 'Violin-Modes,' of the silica suspension fibres can be excited by earthquakes, sudden relaxations of mechanical stress, etc.; and, with the tension in each fibre being 10 kg.wt., their fundamental modal frequencies are of order 500 Hz, such that they (and their harmonics) may transfer vibrational energy along the line of the beam-axis to their suspended test-masses, at frequencies lying within the gravitational wave detection bandwidth. In vacuum, the fibres' ring-down periods extend over days because of their high Q values (~ 6×10^8) [7], which is unacceptably long because during these dead-times gravitational wave observations cannot be made. It is therefore necessary to monitor and then 'cold-damp' these resonances [8]—in the likely presence of significant additional 'pendulum-mode' motion of the test-masses themselves, and their suspension fibres, as they swing slowly under gravity following such excitations. This is currently a challenge generic to all extant interferometric gravitational-wave detectors. The pendulum-mode frequencies for aLIGO are ~ 0.6 Hz.

The Violin-Mode (*VM*) measuring system, whose novel detectors are described below, has been retro-fitted to an aLIGO test-mass/mirror suspension [9]. Here, the design of its photodiode-based sensor and displacement calibration system are described. The sensor was designed to

measure simultaneously the *VM* signals from all four fibres of a fully-suspended test-mass, with a firm target *VM* displacement sensitivity of 10^{-10} m (rms) per √Hz at 500 Hz, over a (following a change in specification) detection span of ±0.1 mm about the mean position of each fibre. This detection range was specified in order to cater for potential slow drift over time in the mean position of a fibre, due to mechanical relaxation of the supporting structure[†]. Other practical constraints on the detection system were that it should be vacuum compliant, have no moving parts, and function correctly under 0.6 Hz pendulum motion of the suspension fibres, where excited amplitudes of tens of μm, peak-peak, are certainly conceivable. Also, for reasons of security, no physical part of the detection system was to be allowed to approach the fibres too closely, since in practice even a light accidental touch during retro-fitting could cause the highly-tensioned silica fibres to shatter.

After much experimentation, a system of four optical shadow-sensors was chosen as the basis of the Violin-Mode detection system, operating in the Near InfraRed (NIR). In the configuration that was finally adopted each vertically-orientated silica fibre was to be illuminated from one side, somewhat above its mid-plane, by its own steady beam of NIR radiation, as indicated in Figure 1. The vertical shadow cast by each fibre was then to be monitored by a synthesized 'split-photodiode' based sensor—specially designed to detect with high resolution *VM* oscillations of the fibre having a transverse component parallel to the interferometer's beam-axis. The performance of these sensors, which were not simple split-photodiode devices, is the subject of this work. Here, the four suspension fibres of a test-mass, together with their respective sources of illumination (Emitters) and their shadow sensors (Detectors), have been labelled A–D, as indicated in Figure 1.

Within each adjacent pair of aLIGO suspension fibres, (C and A) and (D and B) in the Figure, the fibres themselves are physically separated by a nominal 30 mm (±0.5 mm) measured parallel to the ξ-axis, i.e., parallel to the beam-axis of the interferometer and the cylindrical axis of the test-mass/mirror.

2. The Violin-Mode shadow sensor

Two pairs of 'split-photodiode' *VM* detectors (as shown in Figures 3 and 4) were mounted within a single 'Dual shadow-sensor' housing, so that they were able to monitor simultaneously the *VM* oscillations of a pair of fibres, such as C and A in Figure 1. The detectors designated for fibres B and D were mounted within the similar, separate, housing shown schematically in the Figure.

Violin-Mode oscillations of fibre A parallel to the ξ -axis, as indicated by the double-headed arrow in Figure 1, caused that fibre's shadow to oscillate laterally across the face of 'split-photodiode' detector 'A,' which was recessed behind an aperture in the front-plate of its housing. This detector was mounted internally within the housing so as to be aligned with the right-hand aperture, fibre, and the source of illumination shown in the Figure. Therefore, the oscillating shadow generated within this 'split-photodiode-based' detector a modulated (differential) photocurrent at the *VM* frequency, and this current was converted into an oscillating voltage, which was then amplified, and detected. Within their Dual shadow-sensor housings, detectors 'C' and 'A' (and, likewise, 'B' and 'D') were separated by a horizontal pitch of 30.0 mm. The four separate LED-based sources of illumination, one per fibre, were designed to be angled in azimuth (±1.5º), in order to compensate for variations in the nominal '30 mm' pitch of the suspension fibres themselves, so as to realign the shadow of each fibre onto the centre of its respective 'split-photodiode' shadow detector.

[†] The original specification, before the 'de-scope,' was ±0.5 mm: i.e., a dynamic range of 140 dB.

2.1. The shadow-sensor system designed for an aLIGO suspension

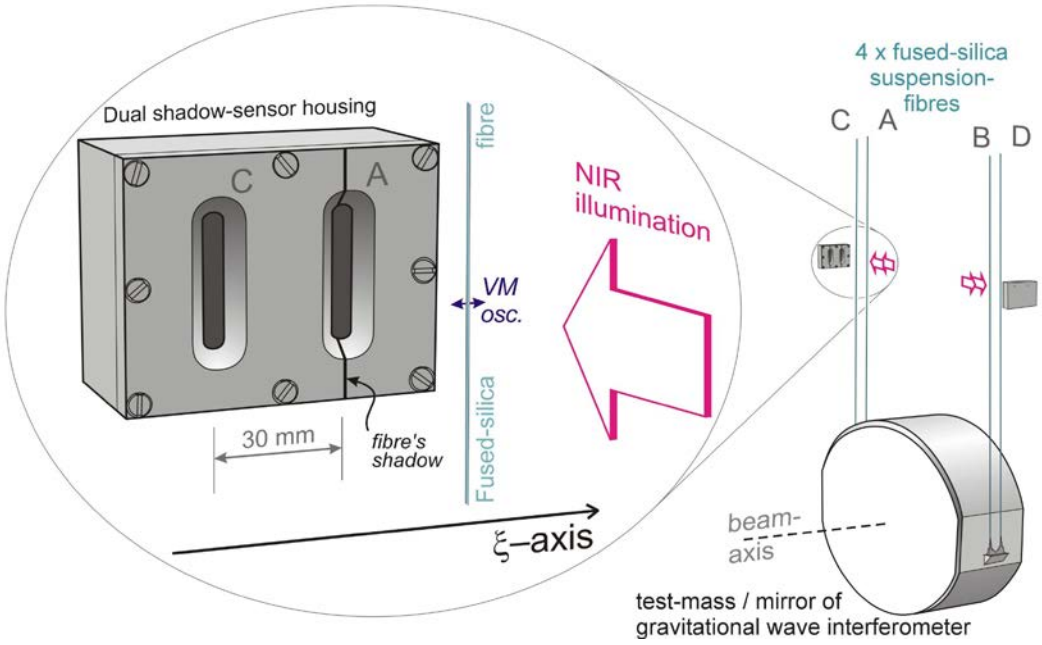

Fig.1. The aLIGO suspension system for a 40 kg test-mass/mirror comprises four fused-silica suspension fibres, arranged in two pairs across the 340 mm diameter of the test-mass. Here, the paired fibres have been labelled (C, A) and (B, D). For clarity, the enlargement in the schematic shows only fibre 'A' of the (C, A) pair, together with its collimated source of NIR illumination (λ = 890 nm). The resulting shadow cast by this fibre falls over the right-hand aperture in the front-plate of the Dual shadow-sensor housing 'C-A' of this work, as indicated, as well as over an internally-mounted 'split-photodiode' sensor. Similarly, the shadow of fibre C would fall over the left-hand aperture in the housing's front-plate, and over its respective internally-mounted sensor. Here, the ξ-axis, and the monitored *VM* oscillation of the fibres—marked in the Figure by the double-headed arrow for fibre A—would be parallel to the interferometer's beam-axis. Such oscillations would be transferred to the fibres' shadows without any lateral magnification. The cylindrical aLIGO suspension fibres measure 600 mm long by 400 μm in diameter.

The physical stand-off distances of the Dual shadow-sensor housings from the fibres was set at 12.5 mm, placing the detectors themselves at some 74 fibre diameters away from the fibres' axes. However, as discussed below, the stand-off distance could have been increased to 20 mm for both detectors and emitters without loss of—indeed with a modest gain in—sensitivity to *VM* fibre oscillations.

Each source (Emitter) of Near InfraRed radiation for illuminating the silica fibres comprised 8 × OP224 'pill' package miniature LEDs (λ = 890 nm), which incorporated 1 mm diameter lenses, stacked above one another so as to form an approximation to a linear source (column) of light, the LEDs' axes of emission being horizontal. The overall physical height of the LED columns was 26 mm, so that they were fairly well matched to the photodiode (PD) shadow sensors described below, which were 29.1 mm tall. The series-connected LEDs in each source were supplied by a constant current of approximately 25 mA (stable to ±1 μA, the maximum continuous currents for OP224s being 100 mA), and, when active, each source created at its respective split-sensor a horizontally-directed beam of NIR illumination in—essentially—a vertical plane. This light was collimated further by an 80 mm Focal Length plano-convex spherical lens, placed within each Emitter housing between the column of LEDs and the illuminated fibre. For security, the stand-off distance between each fibre and the front face of its Emitter was chosen to be 15 mm. The resulting average irradiance at each sensor element was 2.8 $W.m^{-2}$.

2.2. Shadow detection theory

The required *VM* displacement sensitivity of 10^{-10} m (rms) per √Hz at 500 Hz for a simple shadow-sensor proved quite challenging, and it soon became clear that such a sensitivity would not be achieved easily if the (preferred) unmodulated source of illumination were to be used. Conventional, effectively triangular, split-photodiode shadow sensors were tried at the outset of this work, but although they were found to have adequate span to compensate for fibre drift (±0.5 mm originally, and ±0.1 mm following a de-scope), they did not possess at the same time sufficient displacement sensitivity—by a factor > 30. In fact, the two rectangular PD elements which eventually were employed in each detector were aligned with, rather than being skewed relative to, the orientation of their fibre's shadow. As in a conventional split-photodiode detector, they were used in differential pairs in order to increase sensitivity to (shadow-) displacement, whilst, at the same time, providing some degree of common-mode rejection. Here, however, the two, separate, PD elements were synthesized into a single 'split-PD' detector.

In what follows the two contiguous side-by-side elements of each detector are labelled PDa (left-hand element) and PDb (right-hand element), and the following analysis was made in order to determine the best shape/size of PD for each sensor element. These factors turned out to have a profound influence on the detector's sensitivity to shadow displacement.

The silica fibres' shadows were in fact narrower in the plane of each detector than the combined lateral (effective) widths of PDa and PDb: 0.95 mm shadow width at a 2% shadow-depth (defined below), *cf* a typical full detector width of 1.72 mm. Therefore, when centred on a split-detector, a fibre's shadow overlapped neither outer edge of its two PD elements. Nevertheless, the analysis below treats initially the more general case of a shadow covering the full width of a single sensor element.

Here, a single rectangular PD sensor is considered, with a moveable linear shadow falling across it, the axis of the shadow (actually, orientated vertically) being parallel to two of the PD's sides. Movement of the shadow across the face of the sensor is considered to be uniform, and at right-angles to the shadow's axis. For this derivation the following identities have been made: -

- The PD's physical detection area (width × height) = $w \times h$ [m^2].
- The irradiance of the illuminating NIR beam at the PD (wavelength λ = 890 nm) = I_0 [$W.m^{-2}$].
- The PD's responsivity at the above wavelength = r [$A.W^{-1}$].
- The depth of the fibre's shadow = $g(x)$ — a dimensionless shielding factor varying between 0 and 1, (0 ≡ transparent; 1 ≡ opaque)—considered to be uniform up the shadow's axis. In this treatment the x-axis is imagined to be fixed to the shadow, to move with it, and to be parallel to the ξ-axis shown in Figure 1; and so $g(x)$ describes the shadow's fixed profile as it moves back and forth over the PD sensor—following the movement of the fibre which is casting the shadow.

If the shadow is imagined to be offset from the (vertical) centre-line of the PD element by a variable distance, ξ, as shown in Figure 2, then the shaded PD's photocurrent, $\boldsymbol{i}_{photo}$, is given straightforwardly by: -

$$\boldsymbol{i}_{photo} = \boldsymbol{r}.I_0.h.\left(\int_{-\xi-w/2}^{-\xi+w/2}(1-g(x))dx\right), \tag{1}$$

where the quantity within the brackets is the cross-hatched area shown in Figure 2—the integral over the PD detector's width of that fraction of the incident light reaching the sensor. Therefore, from Equation 1, the rate of change of photocurrent with shadow position is

$$\frac{\partial \boldsymbol{i}_{photo}}{\partial \xi} = \boldsymbol{r}.I_0.h.\frac{\partial}{\partial \xi}\left(\int_{-\xi-w/2}^{-\xi+w/2}(1-g(x))dx\right). \tag{2}$$

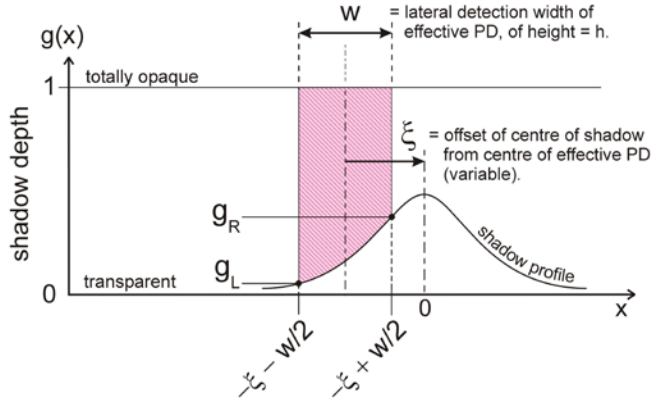

Figure 2. Diagram showing the profile of a silica fibre's shadow as it falls across a photodiode (PD) sensor of effective (horizontal) width w, and vertical height h. For generality, the shadow is shown here covering completely the width of the PD sensor. The vertically-orientated shadow is imagined to be offset horizontally from the centre of its PD by a variable amount ξ (defined in the caption of Figure 1), and to have depths at the left-hand and right-hand edges of the PD of g_L and g_R, respectively.

Using the Leibniz Integral Rule: $\frac{\partial}{\partial\xi}\left(\int_{a(\xi)}^{b(\xi)} f(x,\xi).dx\right) = \int_{a(\xi)}^{b(\xi)} \frac{\partial f}{\partial\xi}.dx + f(b(\xi),\xi).\frac{\partial b}{\partial\xi} - f(a(\xi),\xi).\frac{\partial a}{\partial\xi}$,

to differentiate under the integral sign, allows Equation 2 to be written quite simply as

$$\frac{\partial i_{photo}}{\partial\xi} = r.I_0.h.\{g(-\xi + w/2) - g(-\xi - w/2)\}$$, or, more compactly still as

$$\frac{\partial i_{photo}}{\partial\xi} = r.I_0.h.\{g_R - g_L\}. \quad (3)$$

Here, g_L and g_R are the shadow depths at the left and right edges of the photodiode sensor, as defined in Figure 2. That a detector, such as a bolometer, will only be sensitive to changes at its edges if scanned through a varying incident flux (e.g., a phonon flux in liquid helium) is not a new idea [10], but the foregoing analysis shows that this is formally true also for a shadow detector, with the marginal 'depth of shadow' being the salient parameter.

Moreover, Equation 3 shows that whereas the height h of the PD sensor enters directly into the calculation of raw sensitivity to shadow displacement, its lateral width w does not. Clearly, for the highest displacement sensitivity, and given a certain semiconductor technology (e.g., silicon PDs, with r = 0.6 A.W^{-1}, say), the height h of, as well as the irradiance I_0 at, the PD should be maximized. Furthermore, Equation 3 shows that the difference in shadow depth at the element's edges, and so the sensitivity to displacement, can be maximized by arranging for the shadow to fall over only one edge of the detector—and there along the line of greatest shadow depth. In the case of an illuminated silica glass fibre, the shadow it casts arises from strong angular refraction, and a small amount of reflection, at its cylindrical surface. A well-collimated illuminating beam, from a source of small angular divergence, decreases the unavoidable region of penumbra behind such a fibre, increasing the shadow's depth in the plane of the detector. From Equation 3, this improves in a direct way the sensitivity of the PD sensor to displacement of such a fibre, via its accompanying shadow.

If the photocurrent i_{photo}, of Equation 1 were to flow into a transimpedance amplifier having a fixed transimpedance resistance (gain) R, then, in general, the rate of change of *DC* output voltage V*DC* from such an amplifier with fibre (shadow) position would be, from Equation 3: -

$$\frac{\partial VDC}{\partial\xi} = r.I_0.h.R\{g_R - g_L\}. \quad (4)$$

Here, a positive output voltage has been assumed for an input photocurrent having the sense shown in the Amplifier diagram of Figure 5. Re-writing Equation 4 in the form

$$\frac{\partial \mathrm{V}DC}{\partial \xi} = \frac{\left[r.\mathrm{I}_0.\mathrm{w.h.R}\right]}{\mathrm{w}}\left\{\mathrm{g_R} - \mathrm{g_L}\right\} \tag{5}$$

allows the product of terms within the square brackets of Equation 5 to be identified with the output voltage V*DC* from the amplifier when no part of the shadow falls across the sensor element under consideration. In practice this is a readily measurable quantity, as is the effective physical width w of the detector, in the denominator of Equation 5. Also, a test fibre's shadow profile may be measured by scanning its shadow across a PD detector masked by a narrow slit—giving in this work a typical maximum, cental, shadow depth of $\mathrm{g}(\mathrm{x}) = 0.71$. Equation 5 therefore allows the *DC* 'slope sensitivity'—the rate of change of *DC* output voltage with fibre position—of a particular sensor element to be predicted.

In this work, the two, separate, PDs in each split-detector were synthesized, via reflection, into a single detector, this having two contiguous side-by-side elements—with essentially no dead-band between them. Thus, the shadow depth at the right-hand side of element PDa ($\mathrm{g_R}$), was very closely equal to that at the left-hand side of element, PDb, ($\mathrm{g_L}$), because these elements effectively met along the vertical, central, ridge-line of a beam-splitting mirrored prism, as shown in Figures 3 and 4.

If the separate *DC* output currents arising from the two 'split-photodiode' elements PDa and PDb are written respectively as I_a and I_b, and if the *DC* output voltages arising from them are written similarly as $\mathrm{V}DC,a$ and $\mathrm{V}DC,b$ (please refer to Figure 5), then the preceding text and Equation 4 show that $\partial \mathrm{V}DC,b/\partial\xi = -\partial \mathrm{V}DC,a/\partial\xi$ — provided the fibre's shadow does not fall simultaneously over the outer edge of either detector element. If the shadow depth along the central ridge of the prism is written as $\mathrm{g_{CP}} = \mathrm{g_R}\ (= \mathrm{g_L}$, in this case$)$, then the rate of change of the difference of the *DC* output voltages arising from the two elements with shadow position becomes, from Equation 4, double the magnitude of either sensor element taken separately (assuming *r*, I_0, h, and R are closely the same for the two elements, as they are turned out to be). Thus: -

$$\frac{\partial\left(\mathrm{V}DC,a - \mathrm{V}DC,b\right)}{\partial\xi} = 2r.\mathrm{I}_0.\mathrm{h.R.g_{CP}}. \tag{6}$$

In practice the differential *DC* 'slope sensitivity' of Equation 6 was obtained, by differentiation, from actual measurenments of $\mathrm{V}DC,a$ and $\mathrm{V}DC,b$ as a function of ξ, and from this quantity was inferred for each shadow-sensor its *AC* 'slope sensitivity,' i.e., its absolute calibration in terms of volts (rms) per metre (rms) of fibre displacement—at any desired Violin-Mode frequency. This procedure is described in §3, below. Of course, the resulting *AC* 'slope sensitivity' did not in and of itself allow the actual 'displacement sensitivity' to be determined for a particular vibrating silica fibre and sensor, since this also required knowledge of the noise level in the detection system around 500 Hz—the fundamental *VM* frequency.

However, for frequencies above ~ 10 Hz the transimpedance amplifiers of this work turned out to be shot-noise limited, even at the rather low values of *DC* photocurrent encountered at the PD sensors' bias points: 32–51 μA, for sensors A–D; moreover, the noise over this frequency range from the two sensor elements in each detector was found to be uncorrelated. The measured *DC* photocurrents could be taken to be proportional to (some fraction of) each photodiode's detection area: w × h. Therefore, taking the width w to be a constant across the PD elements, so as to allow selection of a suitable value of h, this fraction was imagined to be a constant for a shadow of fixed width falling at is maximum 'shadow depth' over only one edge of each sensor element. Consequently, the rms shot noise current flowing in each sensor, being proportional to

the square-root of its *DC* bias current, should be proportional to $\sqrt{w \times h}$; but Equation 3 shows that the *DC* (and, hence, *AC*) displacement-signal current should be directly proportional to h. Therefore, taken together, the signal-to-noise ratio for such a sensor was expected to be proportional to $\sqrt{h/w}$.

In consequence, it was decided that for the highest displacement sensitivity 'tall-narrow' photodiodes were to be preferred, and the *Hamamatsu* silicon photodiode S2551, having a detection area of $w \times h$ = 1.2 mm × 29.1 mm, was chosen for each PD element of the Violin-Mode detectors of this work. Because of the way two PD elements were synthesized into a single 'split-PD' shadow-sensor in these detectors, with negligible dead-band between the elements, the average effective width of each element was rather less than the full available PD's width, and it was measured on average to be w = 0.86 mm, yielding, here, a detector element aspect ratio of h/w = 33.8.

2.3. The shadow-sensor for a single silica suspension fibre

The shadow sensor used in this work is shown schematically in Figure 3, and in the schematic and photo of an actual device in Figure 4. Here, the 'split-photodiode' sensor was synthesized from two separate rectangular PD elements by interposing a 45°–90°–45° reflecting prism between them. Split photodiode detectors used as displacement sensors with optical beams, sometimes with shadows, are well known, of course [11,12]. However, in this work it was necessary to have no common anode or common cathode connections between the two PD elements, in order to allow for the separate application of local *AC* feedback to each. This local feedback was used to suppress the effect of the PDs' (and their connecting cables') large capacitance—totalling 600–700 pF—in order to reduce 'noise gain peaking' in their respective transimpedance amplifiers [13].

Figure 3 shows that the sensors were recessed at some distance behind their Detector housing's front-plate—in order (originally) to leave space for internal windows, which were intended to

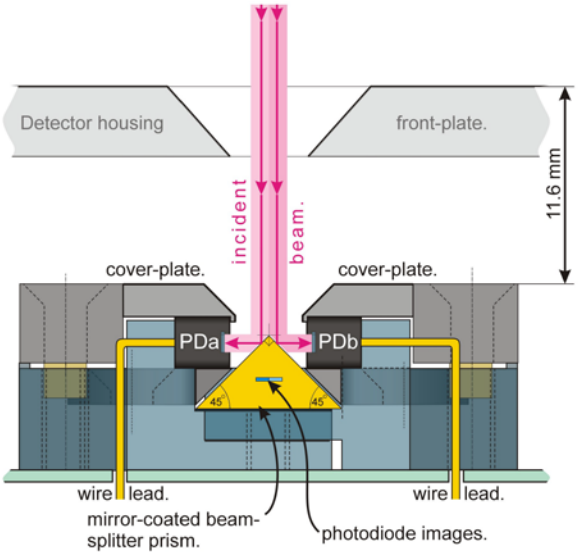

Figure 3. Schematic cross-sectional (plan-) view of a single vertically-orientated split-photodiode based shadow-sensor, drawn to-scale. The two PD elements of each sensor faced each other, separated by a 45°–90°–45° Au/Cr mirror-coated glass prism, which acted as a beam-splitter for the incident NIR beam (and fibre's shadow). As, in the event, no internally-mounted window was used (please refer to the text), the detector housing's front-plate was redundant. Therefore, by removing this plate, and by machining back the casing of the Dual shadow-sensor housing to the level of the cover-plates, the physical stand-off distance from each fibre could have been increased to as much as 24.1 mm, from its nominal value in this work of '12.5 mm,' with no decrease in *VM* detection sensitivity.

cover the two apertures in the front-plate, shown in Figure 1, and to provide a vacuum seal as well. This was also the reason for the reversed chamfer around the apertures in the front-plate, since the internal windows would support better the differential pressure. In the event, because,

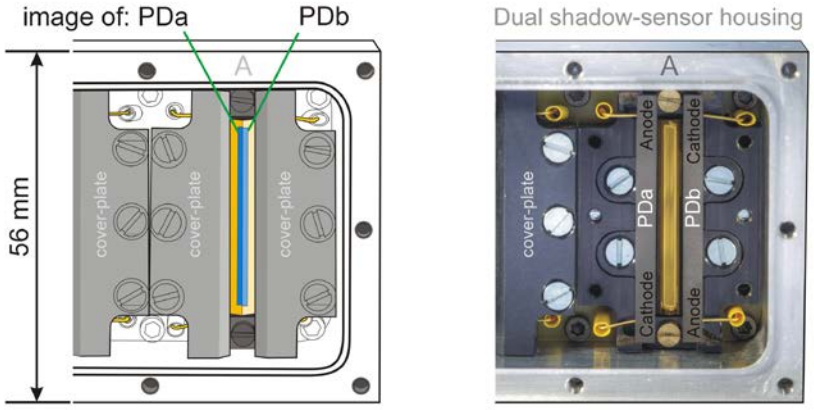

Figure 4. Partial front views of Dual shadow-sensor housing C-A, with its front-plate, bearing the two apertures shown in Figure 1, removed. Here, 'split-PD' shadow-sensor 'A' of the C-A pair of sensors is seen, mounted internally within this housing. Left: schematic of the vertically-orientated shadow-sensor with its cover-plate PD retainers in place, and with the rectangular detection areas of its two 'tall-narrow' contiguous PD elements delineated. Right: photo of this same sensor with its cover-plates removed, showing the underlying *Hamamatsu* S2551 photodiode elements (PDa and PDb) facing each other, and showing the 'split-PD' sensor's composite image in the 45°–90°–45° mirror-coated prism mounted between them (please refer to the schematic in Figure 3). In the photo, the housing's borders (alone) have been outlined, for clarity. In both views a part of shadow sensor 'C' is seen, with its cover-plate still in place, lying immediately to the left of sensor 'A'.

in part, the vacuum-tight sealant that was to be used went out of production, these windows were not mounted—making the front-plates redundant, and also leaving the detectors more remotely positioned from their silica fibres than was necessary. In Figure 3, the incident illuminating beam for each fibre was orthogonal to the base of its respective prism to within ±1.5°.

3. The Violin-Mode amplifier and sensor calibration

Each 'split-photodiode' based shadow sensor was connected to its own detection (transimpedance-) amplifier system, shown in block-diagram form in Figure 5. The detection electronics had three outputs per split-sensor: two *DC* outputs '*VDC*, a' and '*VDC*, b' for photodiode elements a and b, respectively, and a single Violin-Mode *AC* output, '*VM AC,*' derived from the highly amplified difference between PDa's and PDb's *AC* photocurrents. Within the 'Transimpedance Amplifiers' block of Figure 5 the *DC* components of the sensor elements' photocurrents each flowed through transimpedance resistances of value R = 120 kΩ, generating (ultimately) the positive output voltages *VDC*, a and *VDC*, b, respectively, as shown in Figure 5. Lateral (*VM*) oscillation of the fibre and its shadow (oscillating horizontally in the plan-view schematic of this Figure) caused a modulation of the total photocurrents with a 180° phase shift between them. The *AC* components i_a and i_b (= $-i_a$) flowed, however, through separate transimpedance resistances of value R = 1.2 MΩ within the 'Transimpedance Amplifiers' block, generating with this phase-shift the intermediate voltages *VAC*, a and *VAC*, b, shown in the Figure. The difference between these voltages was amplified by a differential gain of approximately ×100, generating the final Violin-Mode *AC* output signal, *VM AC*. Therefore, for each photodiode element separately, the effective *AC* transimpedance gain was a resistance of R = 120 MΩ, i.e., ostensibly 1000× the *DC* transimpedance gain for that element (the narrow passband of the amplifier reduced this figure, slightly, as discussed below).

The known ratio of *AC* to *DC* gain at any *VM* frequency then allowed the Violin-Mode '*AC* slope-sensitivity' to be calibrated for each sensor, as follows. First of all, a vertically orientated 400 μm diameter silica fibre sample was translated (in the ξ-direction of Figure 1), at a constant rate of a few tens of μm per second, using a *DC*-motor driven leadscrew—so as to pass

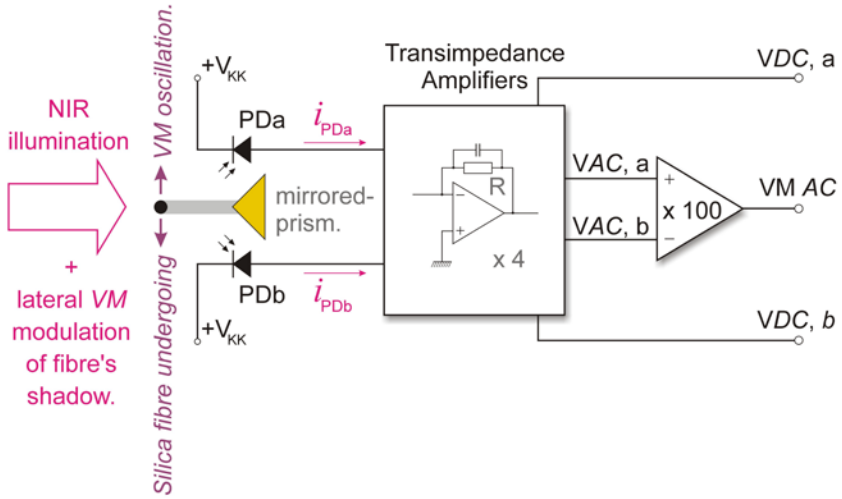

Figure 5. 'Plan view' schematic of the *VM* shadow-sensor and its Transimpedance Amplifiers for an individual silica suspension fibre. The collimated Near InfraRed beam illuminating the suspension fibre from the left fell, together with the shadow of that fibre, across the facing ridge of the 45°–90°–45° Au/Cr mirror-coated beam-splitting prism. The reflected (split) NIR beam then fell onto the reverse-biased (V_{KK} ~ 0.5 V) photodiode elements PDa and PDb, generating in these elements total photocurrents $i_{PDa} = I_a + i_a$ and $i_{PDb} = I_b + i_b$, respectively. Here, $I_{a,b}$ and $i_{a,b}$ represent, in that order, the *DC* and *AC* (Violin-Mode) components of the photocurrents: they were amplified separately to yield the (positive) *DC* output voltages V*DC*,a and V*DC*,b (via R = 120 kΩ), and the intermediate *AC* voltages V*AC*, a and V*AC*, b (via R = 1.2 MΩ), in natural anti-phase. The difference between these latter voltages was further amplified by a factor of 100 to yield the single Violin-Mode *AC* output, *VM AC*.

transversely through the illuminating beam of a particular sensor. The position of the fibre was recorded continuously using a *Renishaw* LM10 magnetic position encoder, having a 1 μm resolution, together with a microcontroller-based interface to eliminate jitter at low translation-rates. The detector's two *DC* voltages, V*DC*, a and V*DC*, b, were recorded simultaneously at every 1 μm step, with 12-bit resolution, using a National Instruments USM-6259 DAQ device, controlled by a LabView data acquisition program running on a Laptop PC. The detector's *DC* output voltages were then plotted as a function of fibre position, producing a pair of 'shadow-notch' traces for each sensor, such as those shown in Figure 6—here, for Emitter-Detector pair A. These two signals were then differentiated off-line with respect to fibre position, ξ, generating in this case the pair of traces shown in Figure 7. Differencing these two traces generated the (differential) '*DC* slope sensitivity' shown in Figure 8, again for sensor A.

Finally, the *AC* 'Violin-Mode' displacement slope sensitivities were found by multiplying the *DC* slope sensitivities by the actual ratio of the *AC* to *DC* transimpedance gains (= 904 ± 4 at 500 Hz, for example—and 976 ± 4 mid-band, at 1.48 kHz). The –3 dB frequencies of the *VM AC* amplifiers were 226 Hz, and 8.93 kHz : the '*VM* bandwidth,' with –40 dB/decade roll-offs below and above these two frequencies, respectively (the upper 3 dB point was reduced in later work to 4.81 kHz, because 8.9 kHz was felt to be unnecessarily high). In this way, the amplifier's *AC* response at the test-mass pendulum-mode frequency (0.5 Hz) was made negligibly small—a factor of 98.9 dB lower than at the expected fundamental Violin-Mode frequency of 500 Hz, in fact. Thus, pendulum-mode oscillation at the level of even tens of μm_{rms} do not affect *VM* detection at ≥ 500 Hz [9].

4. *DC* and *AC* (Violin-Mode) 'slope sensitivity' results

Following the calibration procedure set out in §3, the *DC* and *AC* 'slope sensitivities' for the four shadow sensors, as measured at their ±100 μm measurement points, were found to be as set out in Table 1. The slope-sensitivity (fibre displacement-sensitivity) for Emitter-Detector pair A was found to be lower than that of the other three sensors, this being attributable entirely to the lower irradiance from Emitter A (approximately 20% lower than from the other three Emitters).

Table 1: The calibrated *DC* and *AC* (Violin-Mode) slope sensitivities for the four shadow sensors, A–D. The uncertainties in the tabulated figures, arising from off-line calculation of the slopes, are estimated to be ±1%.

Emitter-Detector pair	*DC* slope sensitivity at ±100 μm. [$kV.m^{-1}$]	*AC* (Violin-Mode) slope sensitivity at $\xi = \pm 0.1$ mm, and 500 Hz. [$MV_{rms}.m_{rms}^{-1}$]
A	9.15	8.27
B	10.77	9.74
C	11.72	10.59
D	11.06	10.00

For each Emitter-Detector pair the *VM* output's *AC* noise Power Spectral Density (PSD) was measured as a function of frequency, using an SR785 Dynamic Signal Analyzer. The frequency range that was covered spanned 0.1 Hz–100 kHz, and, with the fibre removed, the measured noise followed the theoretical bandwidth of the *AC* amplifier very closely indeed down to ~ 10 Hz, below which 1/f noise began to dominate. With the silica test fibre positioned at the $\xi = \pm 100$ μm points the noise value obtained was typically -64.0 ± 0.5 dBV(rms) /√Hz, at 500 Hz [14]. Thus, the *AC* noise PSD was 0.632 ± 0.036 mV_{rms} at the *AC* output of the *VM* amplifier, at 500 Hz; however, using the *AC* 'conversion' slope sensitivities given in Table 1, the voltage noise level could be translated into an equivalent displacement noise. This was taken to be the conservative detection limit for each sensor, at unity (highly-coherent, rms) signal to (random, rms) noise.

Following the methodology described above, the Violin-Mode sensitivities at 500 Hz were found to be as shown in Table 2, the dominant uncertainties arising from the noise measurements, themselves.

Table 2: The *AC* (Violin-Mode) displacement sensitivities at end-of-range positions ($\xi = \pm 0.1$ mm) for the four shadow sensors, A–D, at 500 Hz.

Emitter-Detector pair	*AC* (Violin-Mode) displacement sensitivity @ ±0.1 mm, and 500 Hz. [picometres (rms) / √Hz]
A	76 ± 5
B	65 ± 4
C	60 ± 4
D	63 ± 4

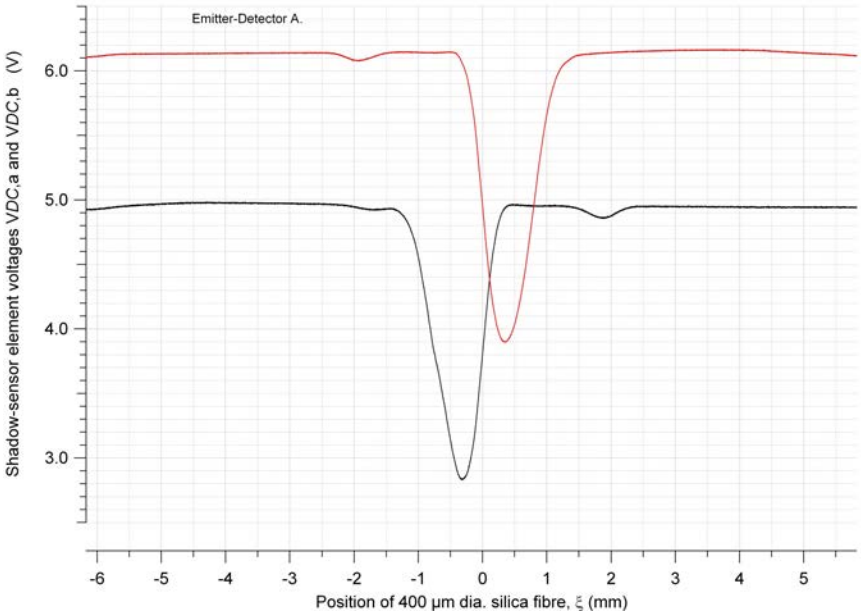

Figure 6. The *DC* photodiode outputs for Emitter-Detector A: V*DC*, a (lower trace) from photodiode element PDa, and V*DC*, b (upper trace) from photodiode element PDb, as a 400 µm diameter silica test fibre was scanned slowly in the ξ-direction (the origin of the abscissa in this Figure was the location of the dividing-ridge of the beam-splitting prism). In this Figure the fibre's shadow fell first over PDa and then over PDb, as its position ξ was increased slowly, causing successively 'notches' in the *DC* outputs from these two detector elements. The difference in mean *DC* levels for the two traces was due to the slightly different detection widths 'w' of these elements (please refer to §2.2, Equation 5).

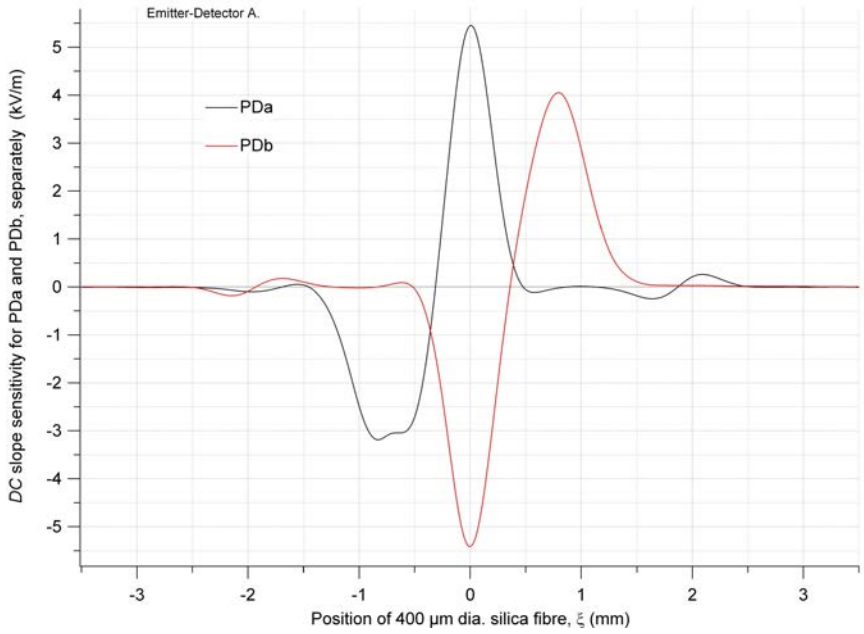

Figure 7. Spatial derivatives $\partial VDC,a/\partial\xi$ and $\partial VDC,b/\partial\xi$ (i.e., displacement sensitivities with respect to fibre position, ξ) of the 'shadow notch' traces of Figure 6. The origin of the abscissa denotes the position of the ridge of the beam-splitting mirrored prism. Here, the extremal '*DC* slope-sensitivity' for photodiode element PDa was approximately +5.4 kV.m^{-1}, whilst that for PDb was –5.4 kV.m^{-1}, as expected from the theory of §2.2. Note that the central prism-ridge divider for the two PD detection elements gave rise to significantly larger, and more regular, *DC* slope sensitivities than at the positions where the fibre's shadow fell primarily over the outer edges of the two PD elements—which were located at approximately ±0.8 mm. Comparing the absolute slope-sensitivity values at these locations with those at the central prism-ridge showed the latter to be more than 50% larger, on average.

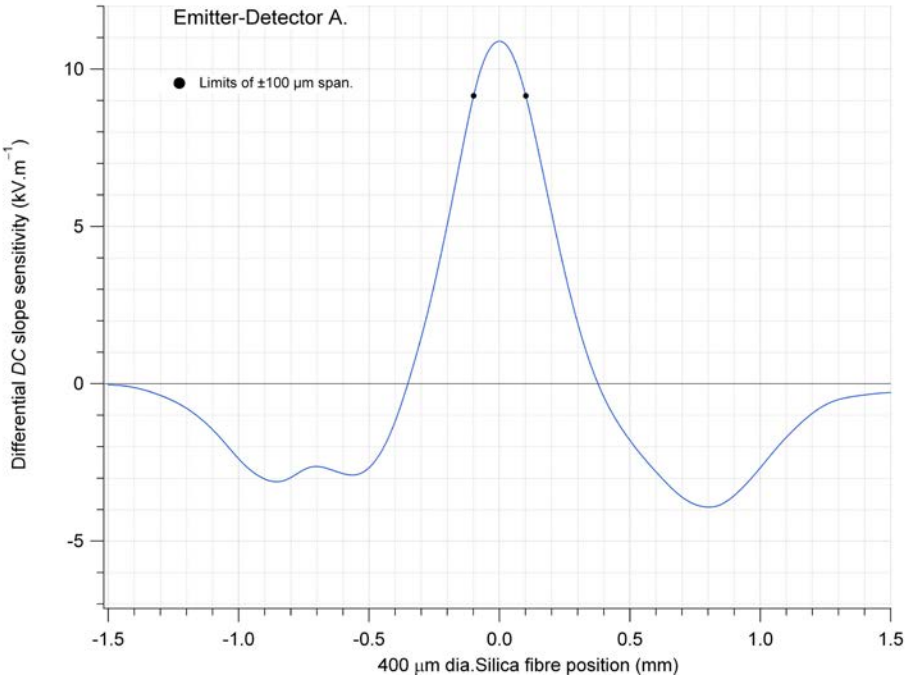

Figure 8. Here, the peak differential *DC* 'slope sensitivity' was found to be approximately 10.8 kV.m^{-1} for Emitter-Detector A. However, at the limits of the required ±0.1 mm span for *VM* detection (shown by the two points in the Figure) the *DC* slope sensitivity was found to be 9.15 kV.m^{-1}. It is the displacement sensitivity at these 'end-of-range' points which is quoted in this work. For Emitter-Detector A the Violin-Mode *AC* displacement 'slope sensitivity' was therefore $904 \times 9.15 \times 10^3 = 8.27$ MV.m^{-1} for this shadow-sensor, at 500 Hz, and at these end-of-span fibre positions (and obviously somewhat higher, for positions in-between). In fact, this was the least sensitive of the four shadow-sensors that were tested—as shown in Tables 1 and 2.

Clearly, even the worst of the shadow-sensors (sensor A) exceeded the target sensitivity of 10^{-10} m_{rms} / √Hz at the ±0.1 mm points—and at all points along the required detection range, in-between.

Further tests of the slope-sensitivities were made more recently with both the fibre-to-Emitter and fibre-to-Detector housing stand-off distances made a symmetrical 20 mm, in the latter case this distance being measured (more reasonably) to the front of the 'cover-plates' shown in Figures 3 and 4—with the Detector housing front-plates removed. Although these results are preliminary, taken overall the four *VM* detectors were found to be approximately 10% *more sensitive* in this symmetrical configuration than in the earlier asymmetrical one, whose results are given in Tables 1 and 2. The cause, which is still under investigation, seems to be that the fibres' shadows (now sharper, and so more 'rectangular') are in this case deeper at their ±0.1 mm points, relative to their centres—leading to greater *VM* sensitivity at these points. In this configuration the shadow-sensors were located 63.75 fibre diameters behind the fibres' axes.

5. Comparison with Theory

The theoretical *DC* slope sensitivity of each of the four shadow sensors is given by Equations 5 and 6. In order to test this theory at the ±100 μm points, the *DC* voltages $V_{DC,a}$ and $V_{DC,b}$ were measured with the fibre's shadow far removed laterally from each sensor—giving the quantity in the square brackets in Equation 5. The widths of each of the eight PD sensor elements (w in the denominator of the equation) were measured between the ridge of the prism and the inside edge of each PD's metallised outer top contact. Finally, the shadow depths $g(x)$

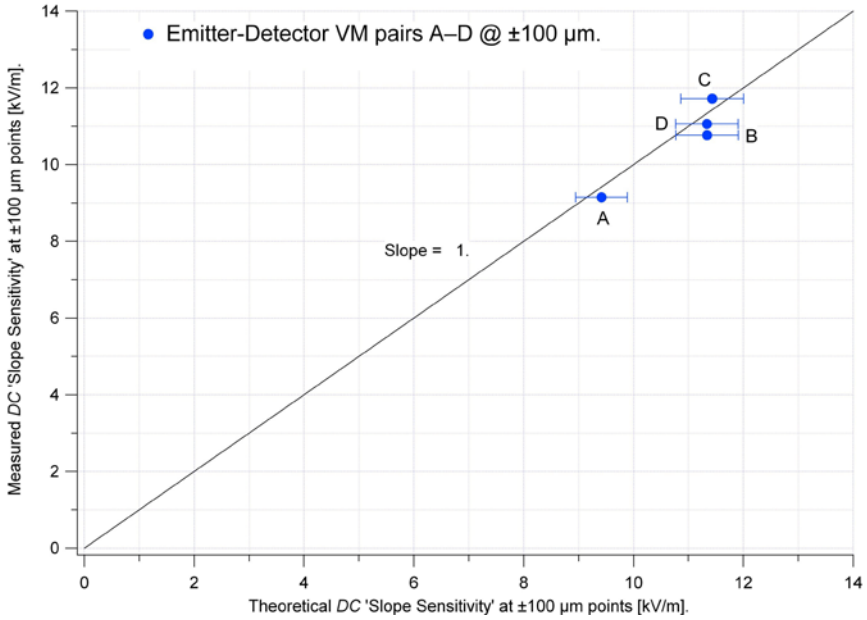

Figure 9. Comparison of the measured and expected *DC* slope sensitivities from the four sensors, the expected values being calculated using Equation 5.

at the ridge of the prism, with the test fibre at the $\xi = \pm 100$ µm points, were taken from the shadow profile measurement described above, yielding non-central values of 0.685 and 0.671, respectively. The *DC* slope sensitivities for the paired elements in each sensor were then summed, giving a value for the expected sensitivity of the sensor, as a whole. Comparison between the expected and measured *DC* slope sensitivities is shown in Figure 9. Note that the dominant theoretical error arose from uncertainty in knowledge of the small effective detector element widths, w (average physical width A–D = 0.86 ± 0.04 mm). Given this uncertainty, the agreement between theoretical displacement 'slope sensitivity' and measurement is seen to be good.

6. First practical Violin-Mode detection results

The shadow-sensors of this work were tested firstly on two silica suspension fibres of a test-mass, this being semi-suspended in air at the Institute for Gravitational Research (IGR), at the University of Glasgow. Here, a 40 kg aluminium dummy test-mass was resting on its lower supporting stops, with a residual tension left in its two attached suspension fibres (B and D)—both of these adjacent fibres being located on the same side of the test-mass. The tension in each fibre was estimated to be approximately one quarter of its nominal fully-suspended value of 10 kg.wt. The results are shown in Figure 10, where the fundamental Violin-Mode resonances of these suspension fibres are clearly seen, closely spaced around 242.5 Hz, with very similar average vibrational amplitudes of 1.21 ± 0.08 nanometres, rms. Subsequently, the complete *VM* detection system comprising sensors A–D was retro-fitted to a similar, but in this case fully-suspended, 40 kg test-mass at MIT. Here, all four suspension fibres were subjected to a far higher tension, yet *VM* resonances were seen in all of them, shadow-sensor B (for example) detecting a 430 (± 30) picometres, rms, resonance, at a frequency of 500.875 Hz [9]. The conversion from measured *AC* volts (rms) to metres (rms) was carried out in both cases using the individual *AC* calibration factors of Table 2 for the sensors, suitably corrected for amplifier roll-off over the frequency range 200–300 Hz for the measurements made at the IGR.

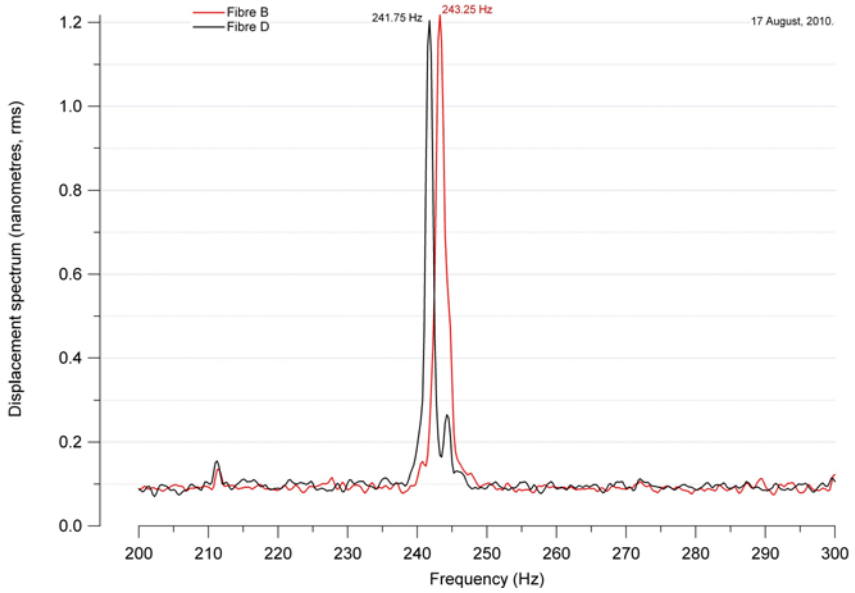

Figure 10. Violin-Mode resonance signals recorded, using the shadow-sensors of this work, on the two silica fibres of a semi-suspended aluminium test-mass at the University of Glasgow (Institute for Gravitational Research). Here, the test-mass was resting on its lower supports, with a residual tension of approximately 2.5 kg.wt. in suspension fibres B and D. The closely spaced fundamental Violin-Mode resonances of these two fibres are clearly seen, at 241.75 Hz, and 243.25 Hz. The spectra were the averages over 50 time samples.

The Violin-Mode resonances shown in Figure 11 and in reference [9] were certainly excited acoustically by airborne noise in the Lab, as well as by vibration through the Lab's floor.

7. Conclusions

All four 'split-photodiode' Violin-Mode (*VM*) detectors exceeded the required target for aLIGO of 10^{-10} m_{rms} / √Hz, over a detection span of ±0.1 mm, as shown in Table 2. This was achieved over a *VM AC* bandwidth of 226 Hz–8.93 kHz (–3 dB points), in fact, so that the available *VM* bandwidth encompassed up to ~ 10 harmonics of a suspension fibre's fundamental violin Eigenmode. At the same time, these *VM* detectors were indeed unaffected by tens of μm_{rms} 'pendulum-mode' motion of an interferometer's test-mass, at ~ 0.6 Hz [9]. The sensor having the lowest sensitivity (A) suffered from an abnormally low irradiance from its particular illuminating source. Perhaps a batch of low radiant flux LEDs had been used inadvertently, here, since the other three sensors exhibited very similar irradiances and displacement sensitivities? Using detectors B and D, *VM* resonances having very similar vibrational levels of 1.2 nm_{rms} were measured straightforwardly in the silica fibres of a dummy test-mass suspension; and a resonance of 430 pm_{rms} was observed using detector B in a more highly tensioned fibre.

The theory of sensitivity to shadow displacement, developed here, was a good predictor of sensitivity for all four of the detectors at their ±0.1 mm points. It led directly to a high sensitivity to fibre (shadow) displacement through the use of 'tall-narrow' photodiode elements, synthesized into 'split-PD' detectors. Crucially, the use of beam-splitting prisms in these detectors increased their displacement sensitivities by some 50% over the sensitivities available at their physical edges (as per conventional split-PD detectors)—as seen in Figure 7. It is conjectured that this gain arose from actually detecting shadow displacement well away from the detection margins of the photodiode elements.

Taking the performances of the four shadow-sensors as a whole [giving a *VM* sensitivity range of (69 ± 13) pm_{rms} / √Hz, at 500 Hz], it is unclear how the present design of these sensors could be simplified further, whilst still meeting the target sensitivity of 10^{-10} m_{rms} / √Hz, at 500 Hz.

However, there is still potential for increasing their displacement sensitivity. Using a 1 mW laser diode, whilst carefully avoiding fringing issues, could increase the (rather low), sensor irradiance by a factor ~6, or more. Using even 'taller' sensor elements eventually compromises

the detection of higher harmonics in a 600 mm long fibre, but an increase in detector height to 60 mm should be feasible; and, as mentioned in §4, by moving to a symmetrical stand-off distance for the emitters/detectors of 20 mm from their respective silica suspension fibres, the displacement sensitivity can be increased by a modest 10%. Thus, taken together, a displacement sensitivity of ~ 20 pm_{rms} / √Hz ought to be achievable, from 500 Hz—5 kHz.

At the time of writing the Violin-Mode sensor system described here has not been adopted for aLIGO, and, in fact, the issue of vacuum compatibility remains unresolved, because the *Hamamatsu* photodiodes used for the detector elements had been encapsulated, using an epoxy. However, were it to become necessary, the issue of the epoxy for the photodiodes from this, or another, manufacturer probably could be resolved, and the LEDs and other components used are likely to prove vacuum compliant, or have vacuum-compliant alternatives.

8. Acknowledgements

We thank the IGR, University of Glasgow, Scotland, UK, for the silica fibre test samples used in this work, and acknowledge that without the research of Alan Cumming, Giles Hammond and Liam Cunningham of that institution on development and construction of the prototype aLIGO test-suspension used in obtaining the Violin-Mode results reported here, the work reported in this paper would not have been possible. We also thank Ken Strain of that institution for setting the sensitivity, and scope, of this work, and would like to thank Angus Bell of the IGR for assistance with the Violin-Mode measurements made on the IGR's aluminium test-mass suspension. Thanks go to Norna Robertson and Calum Torrie of Caltech and the IGR, Dennis Coyne of Caltech, Peter Fritschel, David Shoemaker, Rich Mittleman, and Brett Shapiro of MIT, Alberto Vecchio of the University of Birmingham, and Justin Greenhalgh of the CCLRC (RAL), for their oversight of, and assistance with, this work. We are grateful to the staff of the Physics Department's Electronics Workshop, and the Science Faculty's Mechanical Workshop, at the University of Strathclyde, for their careful construction of most of the component parts used in this work, and we would like to thank *ICOS Ltd.* for manufacture of the beam-splitting prisms. Finally, we are grateful for the support of grant STFC PP/F00110X/1, which sustained this work.

References

[1] Harry G M (for the LIGO Scientific Collaboration) 2010 Advanced LIGO: the next generation of gravitational wave detectors. *Class. Quantum Grav.* **27** 084006 (12pp).

[2] Abbott B P *et al* 2009 LIGO: The Laser Interferometer Gravitational-Wave Observatory *Rep. Prog. Phys.* **72** 1–25.

[3] Raab F J *et al* 2004 Overview of LIGO Instrumentation *Proceedings of SPIE* **5500** 11–24 (29 Sept.).

[4] Aston S M *et al* 2012 Update on quadruple suspension design for Advanced LIGO *Class. Quantum Grav.* **29** 235004 (25pp).

[5] Heptonstall A *et al* 2011 Invited Article: CO_2 laser production of fused silica fibres for use in interferometric gravitational wave detector mirror suspensions *Rev. Sci. Instrum.* **82**, 011301 1–9.

[6] Carbone, L., et al. 2012 Sensors and actuators for the Advanced LIGO mirror suspensions. *Classical and Quantum Gravity* 29 11 115005 (14pp).

[7] Cumming A V *et al* 2012 Design and development of the advanced LIGO monolithic fused silica suspension *Class. Quantum Grav.* **29** 035003 (18pp).

[8] Dmitriev A *et al* 2010 Controlled damping of high-Q violin modes in fused silica suspension fibres. *Class. Quantum Grav.* **27** 025009 (8pp).

[9] Lockerbie N A *et al* 2011 First results from the 'Violin-Mode' tests on an advanced LIGO suspension, at MIT. *Class. Quantum Grav.* **28** 245001 (12pp).

[10] NAL was first alerted to this fact by A.F.G Wyatt, FRS, circa 1973.

[11] Ke-Xun Sun *et al* 2009 Modular Gravitational Reference Sensor Development *Journal of Physics: Conference Series* **154** 012026 (8pp: Differential Optical Shadow Sensor).

[12] Graeme J G 1996 Photodiode Amplifiers. *McGraw Hill* ISBN 0-07-024247 (p221 *et seq*).

[13] As reference[12], but p78.

[14] Lockerbie N A, Tokmakov K V, and Strain K A 2014 A source of illumination for low-noise 'Violin Mode' shadow sensors, intended for use in interferometric gravitational wave detectors (Joint, accompanying, paper: *Measurement Science and Technology*: 15pp). TBA